

1 **Dissolution susceptibility of glass-like carbon versus crystalline graphite in high-**  
2 **pressure aqueous fluids and implications for the behavior of organic matter in**  
3 **subduction zones**

4  
5 **Declarations of interest:** none

6  
7 **Author names:**

8 Simone Tumiatì<sup>a</sup>, Carla Tiraboschi<sup>a,b</sup>, Francesca Miozzi<sup>a,c</sup>, Alberto Vitale-Brovarone<sup>c,d</sup>, Craig E.  
9 Manning<sup>e</sup>, Dimitri Sverjensky<sup>f</sup>, Sula Milani<sup>a</sup>, Stefano Poli<sup>a</sup>

10

11 **Affiliations:**

12 <sup>a</sup>*Dipartimento di Scienze della Terra, Università degli Studi di Milano, via Mangiagalli 34, 20133*  
13 *Milano, Italy; [simone.tumiati@unimi.it](mailto:simone.tumiati@unimi.it) (corresponding author)*

14 <sup>b</sup>*Institut für Mineralogie, Universität Münster, Correnstrasse 24, 48149 Münster, Germany*

15 <sup>c</sup>*Sorbonne Université, Muséum National d'Histoire Naturelle, UMR CNRS 7590, IRD, Institut de*  
16 *Minéralogie, de Physique des Matériaux et de Cosmochimie, IMPMC, 75005 Paris, France*

17 <sup>d</sup>*Dipartimento di Scienze della Terra, Università degli Studi di Torino, via Valperga Caluso 35,*  
18 *10125 Torino, Italy*

19 <sup>e</sup> *Department of Earth, Planetary and Space Sciences, University of California, Los Angeles,*  
20 *California 90095-1567, USA*

21 <sup>f</sup>*Department of Earth & Planetary Sciences, Johns Hopkins University, Baltimore, MD 21218, USA*

22

23 **Abstract:**

24 Organic matter, showing variable degrees of crystallinity and thus of graphitization, is an important  
25 source of carbon in subducted sediments, as demonstrated by the isotopic signatures of deep and  
26 ultra-deep diamonds and volcanic emissions in arc settings. In this experimental study, we  
27 investigated the dissolution of  $sp^2$  hybridized carbon in aqueous fluids at 1 and 3 GPa, and 800°C,  
28 taking as end-members i) crystalline synthetic graphite and ii) X-ray amorphous glass-like carbon.  
29 We chose glass-like carbon as an analogue of natural "disordered" graphitic carbon derived from  
30 organic matter, because unlike other forms of poorly ordered carbon it does not undergo any  
31 structural modification at the investigated experimental conditions, allowing approach to  
32 thermodynamic equilibrium. Textural observations, Raman spectroscopy, synchrotron X-ray  
33 diffraction and dissolution susceptibility of char produced by thermal decomposition of glucose  
34 (representative of non-transformed organic matter) at the same experimental conditions support this

35 assumption. The redox state of the experiments was buffered at  $\Delta\text{FMQ} \approx -0.5$  using double  
36 capsules and either fayalite-magnetite-quartz (FMQ) or nickel-nickel oxide (NNO) buffers. At the  
37 investigated  $P$ - $T$ - $f\text{O}_2$  conditions, the dominant aqueous dissolution product is carbon dioxide,  
38 formed by oxidation of solid carbon. At 1 GPa and 800°C, oxidative dissolution of glass-like  
39 carbon produces 16–19 mol% more carbon dioxide than crystalline graphite. In contrast, fluids  
40 interacting with glass-like carbon at the higher pressure of 3 GPa show only a limited increase in  
41  $\text{CO}_2$  ( $f\text{H}_2^{\text{NNO}}$ ) or even a lower  $\text{CO}_2$  content ( $f\text{H}_2^{\text{FMQ}}$ ) with respect to fluids interacting with  
42 crystalline graphite. The measured fluid compositions allowed retrieving the difference in Gibbs  
43 free energy ( $\Delta G$ ) between glass-like carbon and graphite, which is +1.7(1) kJ/mol at 1 GPa–800°C  
44 and +0.51(1) kJ/mol ( $f\text{H}_2^{\text{NNO}}$ ) at 3 GPa–800°C. Thermodynamic modeling suggests that the decline  
45 in dissolution susceptibility at high pressure is related to the higher compressibility of glass-like  
46 carbon with respect to crystalline graphite, resulting in  $G$ - $P$  curves crossing at about 3.4 GPa at  
47 800°C, close to the graphite–diamond transition. The new experimental data suggest that, in the  
48 presence of aqueous fluids that flush subducted sediments, the removal of poorly crystalline  
49 "disordered" graphitic carbon is more efficient than that of crystalline graphite especially at shallow  
50 levels of subduction zones, where the difference in free energy is higher and the availability of  
51 poorly organized metastable carbonaceous matter and of aqueous fluids produced by  
52 devolatilization of the downgoing slab is maximized. At depths greater than 110 km, the small  
53 differences in  $\Delta G$  imply that there is minimal energetic drive for transforming "disordered"  
54 graphitic carbon to ordered graphite; "disordered" graphitic carbon could even be energetically  
55 slightly favored in a narrow  $P$  interval.

56

## 57 **1. Introduction**

58 The carbon isotopic signature of the upper mantle, transition zone and lower mantle (Stachel et al.,  
59 2002; Cartigny et al., 2004; Palot et al., 2014), and of gaseous  $\text{CO}_2$  emitted from arc volcanoes  
60 (Mason et al., 2017) suggests that organic matter subducted within sediments displays a major role  
61 in the deep carbon cycle (Hayes and Waldbauer, 2006). The dissolution of graphitic carbon in  
62 aqueous fluids due to oxidation or reduction processes (Connolly and Cesare, 1993; Connolly,  
63 1995; Zhang et al., 2018; Tumiati and Malaspina, 2019b) is of primary importance as it governs the  
64 removal of organic matter from the sediments flushed by fluids released from the dehydrating  
65 subducted plate (Schmidt and Poli, 2013). In contrast to carbonates (e.g., Kelemen and Manning,  
66 2015), graphite has long been considered to represent a refractory sink of carbon in the subducting  
67 slab (Plank and Manning, 2019), showing low solubility in metamorphic fluids (Connolly and  
68 Cesare, 1993) and silicate melts (Duncan and Dasgupta, 2017). However, recent thermodynamic

69 models and experiments suggest that graphite can be readily dissolved in subduction fluids  
70 (Manning et al., 2013), stressing for instance the importance of pH (Sverjensky et al., 2014) and of  
71 dissolved silica (Tumiati et al., 2017). However, it is still not known how graphite crystallinity  
72 might affect the compositions of COH fluids in subduction zones.

73 Carbonaceous material in sedimentary rocks metamorphosed under temperature and pressure  
74 conditions characteristic of subduction zones exhibit a progressive increase in crystallinity (e.g.,  
75 Beyssac et al., 2002). Besides exceptional preservations of amorphous-like carbon in some  
76 metamorphic rocks (Bernard et al., 2007), carbonaceous material metamorphosed under prograde  
77 temperature increase to about 550 °C is characterized by a variety of turbostratic structures, from  
78 poorly crystallized to almost crystalline, that are commonly referred to as disordered graphitic C  
79 (Beyssac and Rumble, 2014; Vitale Brovarone et al., 2013; Bollinger et al., 2004)). Carbonaceous  
80 material in high-temperature and ultra-high-pressure terranes is instead characterized by rather  
81 crystalline graphite (Beyssac et al., 2002). Thus, disordered graphitic carbon should represent the  
82 most common form of carbonaceous material under forearc to sub-arc metamorphic conditions  
83 where large amounts of aqueous fluids are released from the slab.

84 Crystalline (ordered) graphite is crystallographically defined by an interplanar  $d$  value of exactly  
85 3.35 Å and a long-range crystalline order with crystallite size of at least a few dozen nanometers  
86 (Luque et al., 1998). The chemical bonds within the layers of hexagonally arranged carbon atoms  
87 are covalent with  $sp^2$  hybridization (Fitzer et al., 1995; Langenhorst and Campione, 2019). The  
88 thermodynamic properties of carbon without long-range crystalline order and of poorly crystallized  
89 and/or defect-rich ("disordered") graphitic carbon are not available at high-pressure and high-  
90 temperature conditions, hence thermodynamic models generally assume perfect ordering and well-  
91 developed crystallinity of graphite. Although some studies suggested that "disordered" graphite and  
92 well crystallized graphite may display different dissolution behavior in aqueous fluids (Ziegenbein  
93 and Johannes, 1980; Connolly, 1995; Luque et al., 1998), others concluded that their  
94 thermodynamic properties must be very similar (McCollom, 2013).

95 In this study, we provide the first experimental results on the high-pressure/high-temperature  
96 dissolution at relatively oxidized conditions of i) ordered crystalline graphite (with crystallite size  
97 around 50 nm determined by synchrotron X-ray diffraction and small Raman "disorder"  $D$  peak)  
98 and ii) X-ray amorphous glass-like carbon, by measuring the CO<sub>2</sub> content of aqueous fluids in  
99 equilibrium with these two  $sp^2$ -hybridized carbon forms. Glass-like carbon is indeed a typical  
100 disordered  $sp^2$  bonded carbon (like graphitic carbon) consisting of randomly distributed curved  
101 graphene layer (also called disordered multilayer graphene, or DMLG) fragments dispersed in an  
102 amorphous matrix (Hu et al., 2017). Glass-like carbon is non-crystalline (X-ray amorphous) and

103 non-graphitizing, meaning that it resists the development of graphite crystals up to 3000°C at room  
104 pressure, and up to 45 GPa at room temperature (Shiell et al., 2018). From a thermodynamic point  
105 of view, glass-like carbon can be considered as a quasi-amorphous or crypto-crystalline solid with  
106 crystallite dimensions smaller than 5–8 nm (Guencheva et al., 2001). In light of these properties, we  
107 used glass-like carbon as an analogue of poorly organized organic matter. The advantage of using  
108 glass-like carbon instead of other poorly crystalline disordered carbon allotropes lies in its  
109 metastable persistence at the investigated experimental conditions (1–3 GPa, 800°C, 12–24h). Other  
110 disordered carbon materials, such as saccharose-based char, are known to recrystallize promptly at  
111 high-pressure/high-temperature conditions (Beyssac et al., 2003), which would prevent  
112 equilibration between fluids and solid carbon in days-long runs, and therefore the retrieval of  
113 thermodynamic parameters. The choice of using glass-like carbon as an analogue for natural  
114 disordered carbon is also supported by comparison of glass-like carbon with char produced by  
115 thermal decomposition of glucose at the same experimental conditions.

116 The experimental results allowed retrieving the difference in Gibbs free energy ( $G$ ) of glass-like  
117 carbon compared to that of crystalline graphite at high pressures and temperatures, demonstrating  
118 that, although small, this difference can lead to substantial changes in dissolved carbon content  
119 predicted by available thermodynamic models that assume a perfectly ordered crystalline state of  
120 graphitic carbon.

121

## 122 **2. Methods**

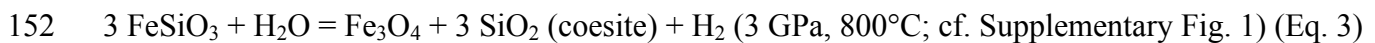
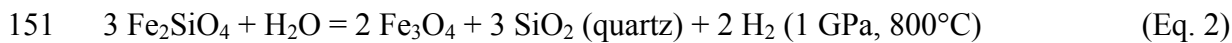
123 In this study, we use the recommended terminology of IUPAC (Fitzer et al., 1995) for the  
124 description of carbon as a solid, which is summarized in the Appendix.

125

### 126 *2.1 Bulk compositions, starting materials and buffering strategy*

127 Fluids in equilibrium with crystalline and disordered  $sp^2$  carbon were generated starting from oxalic  
128 acid dihydrate (OAD;  $H_2C_2O_4 \cdot 2H_2O$ ; Sigma-Aldrich), highly ordered graphite powder (from  
129 spectroscopic-pure rods, gently hand-ground in boron carbide mortar) and glass-like carbon  
130 spherical powder (Alfa Aesar; type I, i.e., produced by firing polymeric precursors at temperatures  
131 below 2000°C). Crystalline graphite and glass-like carbon were characterized by scanning-electron  
132 microscopy, micro-Raman spectroscopy and synchrotron X-ray diffraction. Additionally, two  
133 experiments have been replicated using pure water (MilliQ, boiled while flushed with  $N_2$  to remove  
134 dissolved atmospheric  $CO_2$ ) instead of OAD to check for possible discrepancies. Experiments were  
135 buffered using the double-capsule technique (Eugster and Skippen, 1967) to prevent the direct  
136 contact with the buffering assemblages, with an inner  $H_2$ -permeable  $Au_{60}Pd_{40}$  capsule (OD = 2.3

137 mm) and an outer Au capsule (OD = 4.5 mm). The outer capsule contained H<sub>2</sub>O and either the  
 138 fayalite–magnetite–quartz (FMQ) or the nickel–nickel oxide (NNO) buffers (Fig. 1). Fayalite and  
 139 magnetite have been synthesized at 1100°C in a gas-mixing furnace under reducing atmosphere  
 140 (CO<sub>2</sub>:CO=10:1), starting from stoichiometrically weighted reagent-grade Fe<sub>2</sub>O<sub>3</sub> (Sigma-Aldrich)  
 141 and amorphous SiO<sub>2</sub> from hydrolyzed tetraethyl orthosilicate (Sigma-Aldrich). Natural hyaline  
 142 quartz powder has been used to build up the final FMQ buffering assemblage. NNO buffer was  
 143 prepared by mixing Ni metal powder (Sigma-Aldrich) and green NiO nanopowder (Sigma-Aldrich),  
 144 previously sintered at 1300°C for 24 h under oxidizing atmosphere to prevent grain size-induced  
 145 discrepancies with the accepted free-energy values of the NNO buffer (Mattioli and Wood, 1988;  
 146 O’Neill and Pownceby, 1993). At equilibrium conditions, as long as all the buffering phases are  
 147 present, the chemical potential of hydrogen is expected to be homogeneous in the inner and in the  
 148 outer capsules. In the outer capsule, the hydrogen fugacity ( $f_{\text{H}_2}$ ) is constrained through the  
 149 reactions:



153 In the inner capsule, the equilibration of the COH fluid is accomplished by the  $f_{\text{H}_2}$ -dependent  
 154 coupled reactions (Tumiati et al., 2017):



156 and



158 As a consequence, the initial fluid composition (H<sub>2</sub>O:CO<sub>2</sub> = 1:1 starting from OAD) adjusts its CO<sub>2</sub>  
 159 fraction until equilibrium in  $f_{\text{H}_2}$  is reached between the inner and the outer capsule. The oxygen  
 160 fugacity ( $f_{\text{O}_2}$ ) in the inner capsule (containing mixed H<sub>2</sub>O–CO<sub>2</sub> fluids instead of pure water) is  
 161 constrained indirectly and it will be slightly lower compared to the  $f_{\text{O}_2}$  constrained in the outer  
 162 capsule (containing pure H<sub>2</sub>O) by FMQ and NNO (cf. Luth, 1989) and it is calculated by  
 163 thermodynamic modeling (see Section 2.5 and Table 2), ranging from  $\Delta\text{FMQ} (= \log f_{\text{O}_2}^{\text{sample}} - \log$   
 164  $\log f_{\text{O}_2}^{\text{FMQ}}) -0.5$  to  $-0.8$ .

165 High-pressure pyrolysis of glucose to char has been conducted in unbuffered single Au capsules  
 166 (OD = 3 mm) welded shut after filling with anhydrous glucose (C<sub>6</sub>H<sub>12</sub>O<sub>6</sub>, or CH<sub>2</sub>O) produced by  
 167 dehydration at 70°C (2 h) of  $\alpha$ -D-glucose monohydrate (Sigma Aldrich) (Ponschke and House,  
 168 2011).

169

170 *2.2 Experimental conditions and apparatus*

171 Experiments were performed at 1 and 3 GPa at 800°C using an end-loaded piston-cylinder  
172 apparatus. Capsules were embedded in MgO rods (Norton Ceramics) and inserted in graphite  
173 furnaces surrounded by NaCl and borosilicate glass (Pyrex). At the top of the assembly, a  
174 pyrophyllite–steel plug was placed to ensure the electrical contact. Temperatures were measured  
175 with K-type thermocouples and are considered accurate to  $\pm 5^\circ\text{C}$ . An alumina disk was placed at the  
176 top of the capsule to avoid the direct contact with the thermocouple. Pressure calibration of the  
177 apparatus is based on the quartz to coesite transition according to Bose and Ganguly (1995)  
178 (accuracy  $\pm 0.01$  GPa). Samples were first pressurized at run pressure, then heated to  $T = 800^\circ\text{C}$ ,  
179 with a ramp of  $100^\circ\text{C}/\text{min}$ . Experiments were quenched by turning off the power supply, resulting  
180 in a rate of temperature decline of  $> 40^\circ\text{C}/\text{sec}$ . The double capsules were prepared by peeling off  
181 the outer capsule, then heated at  $110^\circ\text{C}$  in a vacuum oven ( $> 2$  h) to remove any residual water  
182 trapped in the buffer. After the analysis of volatiles (see below), double capsules were mounted in  
183 epoxy resin and polished for scanning electron microscopy and micro-Raman spectroscopy. The  
184 persistence of the buffering assemblages was always verified by means of electron microprobe  
185 analyses. Single capsules containing char derived from the decomposition of anhydrous glucose  
186 were analyzed for volatiles, then opened to collect the sample, which has been analyzed by  
187 scanning electron microscopy, micro-Raman spectroscopy and synchrotron X-ray diffraction.

188

### 189 *2.3 Analysis of solids*

190 Solid carbon in both buffered and unbuffered runs has been characterized by scanning electron  
191 microscopy, micro-Raman spectroscopy and synchrotron X-ray diffraction. Graphite and glass-like  
192 carbon were analyzed both as starting materials and after quench from run  $P$ – $T$  conditions.

193 Quantitative analyses and back-scattered electron imaging of the experimental products were  
194 performed to check the integrity of the buffering mineral assemblages, using a JEOL 8200  
195 wavelength-dispersive (WDS) electron microprobe, at 15 kV accelerating potential, 5 nA sample  
196 current and 1  $\mu\text{m}$  beam size. Standards used were fayalite (Fe), niccolite (Ni) and grossular (Si). A  
197 counting time of 30 s (10 s background) was used for all the elements. Secondary electron imaging  
198 of pyrolytic carbon has been performed at 15 kV and 0.05 nA sample current.

199 Micro-Raman spectra were acquired using the integrated micro/macro-Raman LABRAM HRVIS  
200 (Horiba Jobin Yvon Instruments) of the Interdepartmental Center “G. Scansetti” (Department of  
201 Earth Sciences, University of Torino, Italy). Excitation lines at 532 nm (solid-state Nd laser and 80  
202 mW of emission power) were used with Edge filter and a grating of 600 grooves/mm. Calibration  
203 was performed using the  $520.6\text{ cm}^{-1}$  Si band. The laser power on the sample was set upon the

204 measured materials at 2 mW by the addition of filters. Acquisition times were set at 25 s for 3  
205 accumulations with a laser spot of 2  $\mu$  m.  
206 X-ray Powder diffraction (XRD) data were obtained at XRD1 beamline (Elettra, Trieste, Italy). The  
207 samples were placed in glass capillaries and mounted onto the head of the Huber Kappa  
208 Goniometer installed at the beamline. The data were collected with a monochromatic radiation  
209 ( $\lambda=0.7000$  Å), using a Dectris Pilatus 2M detector. The beam size at the sample was of 0.2×0.7 mm  
210 and the calibration of the set-up geometry was checked with a LaB<sub>6</sub> pattern. Successively, the  
211 images were integrated with Fit2D software package (Hammersley et al., 1995; Hammersley, 1997)  
212 and analyzed using the GSAS EXPGUI software (Toby, 2001).

213

#### 214 *2.4 Analysis of volatiles*

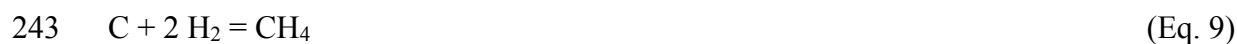
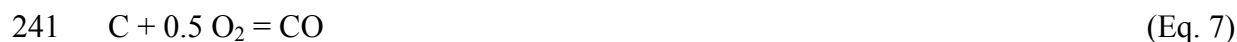
215 For the analysis of quenched volatiles in the capsules (Table 1) we employed the capsule-piercing  
216 technique (Tiraboschi et al., 2016). Volatiles, heated to  $T \approx 80^\circ\text{C}$  to allow liquid water to be  
217 converted into water vapor, were extracted from the capsules in a Teflon reactor and conveyed to a  
218 quadrupole mass spectrometer (EXXTORR 0–200 amu, Mod. XT 200, equipped with secondary  
219 electron multiplier) using ultrapure Ar as carrier gas. The pressure conditions in the reactor were  
220 monitored through high-resolution sensor gauges ( $\pm 1$  mbar precision). The temperature in the  
221 reactor was monitored with K-type thermocouple. Gas mixtures of known compositions and  
222 ultrapure water were utilized for the calibration of the quadrupole mass spectrometer. The technique  
223 enabled retrieval of micromolar quantities of the volatiles H<sub>2</sub>O, CO<sub>2</sub>, CO, CH<sub>4</sub>, H<sub>2</sub> and O<sub>2</sub> with  
224 uncertainties of  $\sim 1$  mol% (10 mol% for CO, due to the interference with atmospheric N<sub>2</sub> on the 28  
225  $m/z$  channel). The periodic analysis of test capsules filled with 1 mg of oxalic acid dihydrate,  
226 thermally decomposed at 250°C to H<sub>2</sub>O, CO, CO<sub>2</sub> and H<sub>2</sub> (Tiraboschi et al., 2016), ensures the  
227 stability and the reproducibility of the analyses over time.

228

#### 229 *2.5 Thermodynamic modeling*

230 The volatile composition of carbon-saturated COH fluids, and in particular their  $X_{\text{CO}_2}$   
231  $[\text{CO}_2/(\text{H}_2\text{O}+\text{CO}_2)_{\text{molar}}]$  in relatively oxidized systems, is dependent on the redox state of the system  
232 (cf. the review of Tumiati and Malaspina, 2019), which can be controlled indirectly in experiments  
233 by fixing the hydrogen fugacity in double capsules (e.g., Eugster and Skippen, 1967).  
234 The fugacities of oxygen and hydrogen in the outer and in the inner capsules at NNO and FMQ  
235 conditions were calculated using the Perple\_X package (Connolly, 2005), using the thermodynamic  
236 dataset of Holland and Powell (Holland and Powell, 1998) revised by the authors in 2004  
237 (hp04ver.dat), the Perple\_X water equation of state (EoS) "H–O HSMRK/MRK hybrid", and using

238 the Excel spreadsheet GFluid (Zhang and Duan, 2010) with the COH fluid EoS of Zhang and Duan  
239 (2009), which is based on the equilibrium constants  $K_P$  of the following reactions:



244 Tumiati et al. (2017) showed that the composition of graphite-saturated COH fluids at 1–3 GPa and  
245 800°C are reproduced best using a modified version of Zhang and Duan's model, implemented with  
246  $f_{H_2}$  coefficients ( $\gamma_{H_2}$ ) changing dynamically as a function of  $X(O)$  [ $=O_2/(H_2+O_2)_{molar}$ ], taken from  
247 the EoS of Connolly and Cesare (1993). Therefore, in this study we refer to this modified model to  
248 i) predict the composition of buffered fluids in equilibrium with crystalline graphite (Table 2); ii)  
249 compare it with the measured composition of fluids in equilibrium with either crystalline graphite  
250 or glass-like carbon (Fig. 2; Table 1) and iii) retrieve the difference in free energy between graphite  
251 and glass-like carbon ( $\Delta G$ ), by iteratively changing the Zhang and Duan's  $K_P$ s (cf. Eqs. 4–7) to  
252 account for the measured  $X_{CO_2}$  of fluids in equilibrium with the latter phase (Table 3). The  
253 experimental  $\Delta G$  was compared with the  $\Delta G$  predicted by thermodynamic modeling, performed  
254 with thermodynamic parameters retrieved from literature added to the database of Holland and  
255 Powell (hp04ver.dat) (Table 4), thus making feasible with Perple\_X the calculation of  $G-P$  and  $\log$   
256  $f_{O_2}(P, T)$  phase diagrams involving glass-like carbon in addition to crystalline graphite.

257 Recent studies outlined the importance of non-volatile charged carbon species (not detectable with  
258 the capsule-piercing technique) and/or organic dissolved compounds in high-pressure COH fluids at  
259 certain  $P-T-f_{O_2}$ -pH conditions ( Sverjensky et al., 2014; Pan and Galli, 2016; Tiraboschi et al.,  
260 2018; Huang and Sverjensky, 2019). In particular, Sverjensky et al. (2014) showed that at high pH  
261 values aqueous bicarbonate and carbonate species become dominant instead of molecular  $CO_2$  and  
262  $CH_4$ . In addition, organic dissolved species (e.g., formates and acetates) may form at ultra-high  
263 pressures (e.g., 5 GPa at 600°C in Sverjensky et al., 2014). Therefore, conventional thermodynamic  
264 models (Connolly and Cesare, 1993; Zhang and Duan, 2009), which consider neutral molecular  
265 species only, are not always adequate to predict carbon speciation in subduction fluids. It is an open  
266 question whether the available thermodynamic models are still valid in the presence of COH fluid  
267 immiscibility, suggested at  $P = 1.5-2.5$  GPa and  $T = 600-700^\circ C$  in graphite-saturated slightly saline  
268 fluids (Li, 2016) and in low-temperature/high-pressure hydrocarbon fluids (Huang et al., 2017). In  
269 particular, Li (2016) found at 2.5 GPa and 700°C at Re–ReO<sub>2</sub> redox conditions ( $\approx \Delta FMQ = +2$ )  
270 mixed H<sub>2</sub>O–CO<sub>2</sub> fluids in equilibrium with almost pure CO<sub>2</sub>. As the capsule-piercing technique  
271 used in our study only allows measurement of the bulk volatile components, it cannot be used to



272 investigate fluid immiscibility. However, on the basis of the results given in our study and in  
273 previous works (Matveev et al., 1997; Carla Tiraboschi et al., 2016; Tumiati et al., 2017), the  
274 conventional models are still able to predict the *bulk* composition (but not necessarily the  
275 speciation) of high-pressure fluids in terms of bulk  $\text{CO}_2/(\text{H}_2\text{O}+\text{CO}_2)$  and  $\text{CH}_4/(\text{H}_2\text{O}+\text{CH}_4)$ , although  
276 they could fail at certain  $P$ - $T$ - $f\text{O}_2$ -pH conditions where species other than  $\text{H}_2\text{O}$ ,  $\text{CO}_{2(\text{aq})}$  and  $\text{CH}_{4(\text{aq})}$   
277 become dominant. In order to justify our experimental approach we used the Deep Earth Water  
278 thermodynamic model (Sverjensky et al., 2014) to confirm that molecular  $\text{CO}_{2(\text{aq})}$  is by far the  
279 dominant carbon-bearing fluid species at our experimental conditions, and to estimate the pH of the  
280 fluids (Table 2).

281

### 282 **3. Results**

283

#### 284 *3.1 Characterization of solid carbon*

##### 285 3.1.1 Crystalline graphite

286 Back-scattered electron observation of graphite powder used as starting material did not reveal any  
287 foreign material. The powder consists of homogeneous flakes with grain size of 10–100  $\mu\text{m}$   
288 (Supplementary Fig. 2 a). X-ray powder diffraction showed that the powder is monomineralic and  
289 crystalline, with a sharp diffraction peak at  $d_{002} = 3.3672 \text{ \AA}$  (Supplementary Fig. 3 - graphite).  
290 Fitted pattern showed that the averaged crystallite size of the sample is around 50 nm. Micro-  
291 Raman spectroscopy of unpolished graphite powder showed a sharp graphite ( $G$ ) peak at  $1600 \text{ cm}^{-1}$   
292 and only a little disorder ( $D$ ) peak at  $1350 \text{ cm}^{-1}$ , confirming that this material is highly ordered  
293 (Ferrari, 2007) (Supplementary Fig. 4). The  $G'$  peak (also called  $2D$  in Ferrari, 2007) at about  $2700$   
294  $\text{cm}^{-1}$  is also well developed. Raman spectra of polished graphite showed a marked increase of the  $D$   
295 peak owing to mechanical modifications during the polishing (Pasteris, 1989), and was therefore  
296 not considered. Quenched graphite samples did not show any evidence of substantial modification  
297 with respect to starting graphite powder, within the uncertainties caused by polishing.

298

##### 299 3.1.2 Glass-like carbon

300 Glass-like carbon spheres used as starting material appeared homogenous at the scanning electron  
301 microscope. They are about  $100 \mu\text{m}$  in size, and show sparse closed porosity (Supplementary Fig. 2  
302 b). X-ray powder diffraction of the spherical powder showed broad peaks, typical of amorphous  
303 materials (Supplementary Fig. 3). Micro-Raman spectra show broad  $G$  and  $D$  peaks, which  
304 characterize amorphous  $sp^2$  carbon (cf. Ferrari and Robertson, 2001), with  $D$  peak  $>$   $G$  peak (Fig.

305 2). The  $G'$  peak is poorly developed. Glass-like carbon retrieved after runs showed Raman spectra  
306 identical to the starting material.

307

### 308 3.1.3 Char from high-pressure pyrolysis of anhydrous glucose

309 Secondary electron imaging of solid carbon formed by decomposition of glucose (char) at 1–3 GPa  
310 and 800°C show microtextures that are dependent on the run duration. In the 12-h run at 1 GPa,  
311 char comes as a loose spherical powder with an average grain size of 1  $\mu\text{m}$  (Figs. 3 a, b). In the 24-h  
312 runs at 1 and 3 GPa, spherical elements are not visible, and char is characterized by a glass-like  
313 appearance with conchoidal fracture and absence of cleavage (Figs. 3 c–f). X-ray powder  
314 diffractions of char (Supplementary Fig. 3) show that the diffraction angle of the most intense peak  
315 is lower compared to that of crystalline graphite, while the full width at half maximum (FWHM) is  
316 higher, meaning a decline of the crystallite size. The crystallite size of char synthesized at the  
317 investigated high-pressure conditions is of about 2–4 nm typical of nano-crystalline materials. The  
318 Raman spectra of char synthesized at 1 and 3 GPa in 24-h long runs are very similar, with broad  $G$   
319 and  $D$  peaks ( $D > G$ ) (Fig. 4). Compared to glass-like carbon, the  $D$  peak is slightly higher, but  
320 broadening of the peaks is a little less pronounced. The  $G'$  peak is comparable to that of glass-like  
321 carbon. The Raman spectrum of char synthesized at 1 GPa in the shorter 12-h run is characterized  
322 by similar  $G$  and  $D$  peaks, but remarkably higher  $G'$  peak (Supplementary Fig. 5), which  
323 characterizes crystalline graphite (Fig. 4).

324

### 325 3.2 Characterization of the fluid phase

326 Volatiles in all the experimental runs have been measured by means of the capsule-piercing  
327 technique (see details in Tiraboschi et al., 2016) (Table 1; Fig. 5; Supplementary Fig. 6). Total  
328 measured volatiles range from 5.51 to 49.5 micromoles in double capsules where fluids were  
329 interacting with either crystalline graphite or glass-like carbon, and from 23.21 to 60.74 micromoles  
330 in single capsules where fluids were produced by complete dehydration of anhydrous glucose due  
331 to the reaction:



333

#### 334 3.2.1 Buffered COH fluids interacting with crystalline graphite

335 Fluids synthesized at 1–3 GPa and 800°C contain mostly  $\text{H}_2\text{O}$  and  $\text{CO}_2$ , with only traces of  $\text{CO}$ ,  
336  $\text{CH}_4$  and  $\text{H}_2$  (typically close to or below the detection limit). At  $P = 1$  GPa,  $X_{\text{CO}_2}$  ( $= \text{CO}_2/\text{H}_2\text{O} + \text{CO}_2$   
337 molar) ranges from  $0.674 \pm 0.007$  ( $f_{\text{H}_2}^{\text{FMQ}}$ ) to  $0.731 \pm 0.008$  ( $f_{\text{H}_2}^{\text{NNO}}$ ). Because the FMQ and NNO  
338 buffers cross at about 1.5 GPa (cf. Supplementary Fig. 1), meaning that the NNO buffer is more

339 oxidizing than FMQ at  $P < 1.5$  GPa and less oxidizing at  $P > 1.5$  GPa, fluids at  $P = 3$  GPa buffered  
340 by NNO are expected to show lower  $X_{CO_2}$  compared to fluids buffered by FMQ (Table 2). At  
341  $f_{H_2}^{FMQ}$ , the run COH76, containing oxalic acid dihydrate (OAD) as starting source of fluid, displays  
342  $X_{CO_2} = 0.74 \pm 0.02$ , and run COH105, containing water instead of OAD, displays a similar  $X_{CO_2}$   
343 of  $0.714 \pm 0.05$ . Instead, at  $f_{H_2}^{NNO}$  conditions the fluid phase is dominated by water, resulting an  
344  $X_{CO_2}$  of  $0.094 \pm 0.001$  in run COH103.

345

### 346 3.2.2 Buffered COH fluids interacting with glass-like carbon

347 Fluids interacting with glass-like carbon at 1–3 GPa and 800°C, buffered by either FMQ or NNO,  
348 contain only traces of CO, CH<sub>4</sub> and H<sub>2</sub>, as in the case of graphite-saturated fluids (Table 1).  
349 However, the fluids with glasslike carbon display different  $X_{CO_2}$  ratios to the graphite-saturated  
350 ones (Fig. 5). In particular, fluids at 1 GPa are display a higher CO<sub>2</sub> content, and are characterized  
351 by  $X_{CO_2}$  of  $0.801 \pm 0.009$  at  $f_{H_2}^{FMQ}$  and  $0.850 \pm 0.006$  at  $f_{H_2}^{NNO}$ , corresponding to a higher content  
352 of +19 and +16 mol% CO<sub>2</sub>, respectively, if compared to graphite-saturated fluids displaying  $X_{CO_2}$   
353 =  $0.674$  at  $f_{H_2}^{FMQ}$  and  $0.731 \pm$  at  $f_{H_2}^{NNO}$  (see above). However, the higher CO<sub>2</sub> compared with  
354 graphite-saturated fluids declines dramatically at 3 GPa. At this pressure, fluids saturated with  
355 glass-like carbon buffered at  $f_{H_2}^{NNO}$  show indeed a  $X_{CO_2}$  of  $0.099 \pm 0.001$ , corresponding to only  
356 +5 mol% CO<sub>2</sub> higher content relative to fluids saturated with graphite displaying  $X_{CO_2} = 0.094$ .  
357 Fluids buffered at  $f_{H_2}^{FMQ}$  conditions show CO<sub>2</sub> content that is even lower than that characterizing  
358 graphite-saturated fluids. In fact, run COH112 is characterized by  $X_{CO_2} = 0.57 \pm 0.01$  ( $0.50 \pm 0.03$   
359 in run COH108, with H<sub>2</sub>O instead of OAD as starting source of fluid), corresponding to a lower  
360 CO<sub>2</sub> content of –24 mol% CO<sub>2</sub> relative to fluids saturated with graphite ( $X_{CO_2} = 0.74$ ; see above).

361

### 362 3.2.3 Unbuffered COH fluids generated by high-pressure thermal decomposition of glucose

363 Fluids produced by high-pressure dehydration of anhydrous glucose display variable compositions,  
364 changing as a function of run time and pressure conditions (Table 1; Supplementary Fig. 6). Fluids  
365 at 1 GPa show high contents of CH<sub>4</sub>, especially in run COH122 characterized by a relatively short  
366 runtime of 12 h. In this run,  $X_{CO_2}$  is  $0.072 \pm 0.001$  and  $X_{CH_4} [=CH_4/(H_2O+CH_4)_{molar}] = 0.261$ .  
367 Fluid in run COH124, characterized by a longer duration of 24 h, displays a higher  $X_{CO_2}$  of  $0.240 \pm$   
368  $0.003$  and a lower CH<sub>4</sub> content ( $X_{CH_4} = 0.056$ ). Fluid at 3 GPa (24 h) is nearly pure water with  
369  $X_{CO_2} = 0.0098 \pm 0.0003$  and  $X_{CH_4} = 0.001$ .

370

## 371 4. Discussion

372 4.1 Comparison between experimental results and available thermodynamic models of fluids in  
373 equilibrium with crystalline graphite

374 The measured compositions of COH fluids interacting with crystalline graphite at 1 GPa and 800°C  
375 (Table 1) is in excellent agreement, in both FMQ- and NNO-buffered experiments, with the  
376 compositions predicted at equilibrium conditions by the modified thermodynamic model of Zhang  
377 and Duan (2009) (Table 2; see details of the model in Section 2.5). At 3 GPa, while the  $fH_2^{FMQ}$ -  
378 buffered fluid matches the composition predicted by the model, the measured composition of the  
379 fluid buffered externally by NNO is characterized by a lower content of  $CO_2$ . The measured  $XCO_2$   
380 would be consistent with an inner-capsule  $\log fO_2$  of  $-12.56$ , instead of the predicted value of  $-$   
381  $11.99$  (Table 2). At this stage, we can only speculate that this could be ascribed to uncertainties  
382 associated to the nickel–nickel oxide buffer (c.f. O'Neill and Pownceby, 1993), which could affect  
383 the estimates of  $fO_2$  and  $fH_2$  imposed by the NNO buffer at 3 GPa.

384 Some recent studies underlined the importance of the variable pH in governing the abundance of  
385 dissolved organic species and charges species (e.g., bicarbonates, carbonates) instead of molecular  
386 species (Sverjensky et al., 2014; Pan and Galli, 2016). Therefore, we used the Deep Earth Water  
387 (DEW) model (Sverjensky et al., 2014) to draw pH vs  $fO_2$  diagrams showing the loci of points  
388 where graphite is stable in COH fluids at saturation conditions at 1GPa–800°C (Fig. 6 a) and 3  
389 GPa–800°C (Fig. 6 b) (black solid lines). The oxygen fugacities expected in COH fluids buffered at  
390  $fH_2^{FMQ}$  and  $fH_2^{NNO}$  conditions are shown for reference. The intersection of these oxygen fugacities  
391 with the graphite-saturation curve represents the investigated experimental conditions (black dots),  
392 and thus provides an estimation of the pH value expected in the synthesized fluids, i.e. 3.5–3.6 at 1  
393 GPa–800°C (neutral pH = 4.02) and 2.22 at 3 GPa–800°C (neutral pH = 3.09). The model predicts  
394 that at the investigated  $P$ – $T$ – $fO_2$ – $fH_2$  conditions the equilibrium between graphite and COH fluids is  
395 thus reached in the  $CO_{2(aq)}$  stability field and at acidic conditions, which prevent the stability of  
396 carbonate and bicarbonate ions.  $CO_{2(aq)}$  is therefore expected to be by far the dominant dissolved  
397 carbon-bearing species, while other C–O–H species should occur in very minor amount, the most  
398 abundant being ethane ( $\approx 10^{-4}$  mol%) at 1 GPa–800°C and formic acid ( $\approx 10^{-3}$  mol%) at 3 GPa–  
399 800°C. Other organic and/or charged species display even lower abundances. This validates the  
400 methodological approach of this study, aiming to retrieve the composition of quenched fluids in  
401 terms of volatile molecular species, assuming that they represent the speciation at run conditions.  
402 As a corollary, the diagrams in Figure 6 suggest that when redox conditions are imposed on a  
403 petrological system (redox-buffered systems), the pH becomes merely a dependent variable, as long  
404 as graphite-saturation conditions persist. Conversely, in pH-buffered systems, the redox state would  
405 be controlled by pH.

406

407 4.2 *Experimental fluids in equilibrium with glass-like carbon and retrieval of its thermodynamic*  
408 *properties at high-pressure conditions*

409 The CO<sub>2</sub> content of fluids interacting with glass-like carbon is different with respect to the CO<sub>2</sub>  
410 content of fluids in equilibrium with crystalline graphite (Fig. 5; Table 1). Fluids at 1 GPa are  
411 considerably enriched in CO<sub>2</sub>, while fluids at 3 GPa are only slightly enriched or even depleted with  
412 respect to graphite-saturated fluids. The observed difference is +19 mol% CO<sub>2</sub> at 1 GPa–*f*H<sub>2</sub><sup>FMQ</sup>,  
413 +16 mol% CO<sub>2</sub> at 1 GPa–*f*H<sub>2</sub><sup>NNO</sup>, +5 mol% at 3 GPa–*f*H<sub>2</sub><sup>NNO</sup> and –24 mol% CO<sub>2</sub> at 3 GPa–*f*H<sub>2</sub><sup>FMQ</sup>.  
414 These different fluid compositions are uniquely ascribable to difference between the  
415 thermodynamic properties of glass-like carbon and crystalline graphite. Taking as example  
416 Equation 6 (C + O<sub>2</sub> = CO<sub>2</sub>), the equilibrium constant of the reaction is:

417 
$$K_p(T) = \frac{[CO_2]}{[O_2]}, \quad (\text{Eq. 11}),$$

418 where brackets indicate equilibrium concentrations of fluid phases over solid carbon.

419 At 1 GPa and 800°C, involving perfectly crystalline graphite, the equilibrium constant of the  
420 reaction following the thermodynamic model of Zhang and Duan (2009) is  $3.416 \times 10^{19}$  ( $\ln K_p =$   
421  $44.98$ ). By changing  $K_p$ , the fluid CO<sub>2</sub> content predicted by the model changes accordingly. By  
422 means of iterative calculation, it is possible to find a  $K_p$  that fits the measured CO<sub>2</sub> value in runs  
423 where fluids reacted with glass-like carbon instead of graphite at the same  $P$ – $T$  conditions. The  
424 equilibrium constant of a heterogeneous reaction with the participation of glass-like carbon (gl)  
425 instead of graphite (graph) can be expressed as:

426 
$$K_{p\text{ gl}}(T) = K_{p\text{ graph}}(T) \exp\left(\frac{\Delta G(T)}{RT}\right) \quad (\text{Eq. 12})$$

427 where  $\Delta G(T)$  is the difference in Gibbs free energy between glass-like carbon  $G_{\text{gl}}(T)$  and graphite–  
428  $G_{\text{graph}}(T)$ , and  $R$  is the gas constant. This difference can be made explicit, resulting in the equation:

429 
$$\Delta G(T) = RT \ln\left(\frac{K_{p\text{ gl}}(T)}{K_{p\text{ graph}}(T)}\right) \quad (\text{Eq. 13})$$

430 As this difference in Gibbs free energy at fixed  $P$ – $T$ – $f$ H<sub>2</sub> must be the same for all the reactions 6, 7  
431 and 9, by means of simulation analysis performed with the Solver tool in the Excel spreadsheet  
432 provided by Zhang and Duan (2010) we changed iteratively all the pertaining equilibrium constants  
433 simultaneously, imposing the mathematical constraint that the resulting  $\Delta G$  is identical for all the  
434 equations, until the model converges to the measured  $X_{\text{CO}_2}$ . The retrieved  $\Delta G$  and the equilibrium  
435 constants retrieved by simulation analysis at 1 and 3 GPa are shown in Table 3.  $\Delta G$  is almost  
436 coincident in runs performed at NNO and FMQ conditions at 1 GPa–800°C, where fluids  
437 equilibrated with glass-like carbon contain higher CO<sub>2</sub> fractions compared to graphite-saturated  
438 fluids. At these  $P$ – $T$  conditions,  $\Delta G$  is equal to +1.6(1) at *f*H<sub>2</sub><sup>NNO</sup> and +1.7(1) kJ/mol at *f*H<sub>2</sub><sup>FMQ</sup>. The

439 difference in Gibbs free energy between graphite and glass-like at 1 GPa agree with previous  
 440 studies performed at room pressure, where  $\Delta G$  is +1.8 kJ/mol at 800°C (Guencheva et al., 2001;  
 441 Gutzow et al., 2005). At 3 GPa and 800°C, fluids in equilibrium with glass-like carbon buffered at  
 442  $f\text{H}_2^{\text{NNO}}$  conditions display a slightly higher  $\text{CO}_2$  content compared to graphite-saturated fluids, and  
 443  $\Delta G$  is equal to +0.5(1) kJ/mol. Fluids buffered at  $f\text{H}_2^{\text{FMQ}}$  conditions show a  $\text{CO}_2$  content which is  
 444 even lower than fluids in equilibrium with graphite, corresponding to a negative  $\Delta G$  of -2.3(2)  
 445 kJ/mol.

#### 447 4.3 Thermodynamic modeling of glass-like carbon and implications for its stability towards 448 graphite and diamond

449 We are not aware of previous Gibbs free energy of glass-like carbon at high pressures, even though  
 450 layers of glass-like carbon spheres have long been employed in experimental petrology as melt  
 451 traps at pressure conditions ranging from 1 to 5 GPa (Robinson et al., 1998; Wasylenki, 2003;  
 452 Dasgupta et al., 2005; Falloon et al., 2008; Spandler et al., 2008). Therefore, we derived the  $G(P, T)$   
 453 curve of glass-like carbon at pressures up to 3 GPa (Fig. 7), by using the following thermodynamic  
 454 parameters (Table 4; Supplementary Table 1):

- 455 • the standard Gibbs free energy of formation, retrieved from the  $G$ - $T$  data of Guencheva et  
 456 al. (2001) and Gutzow et al. (2005) at room pressure and  $T = 298$  K ( $\Delta_f G^0 = 2.357$  kJ/mol);
- 457 • the standard entropy ( $S_{298}^0$ ), retrieved by fitting the  $G$ - $T$  data at room pressure of Gutzow et  
 458 al. (2005). The retrieved  $S_{298}^0 = 6.6$  J/mol/K agrees well with the standard entropy of 6.2  
 459 J/mol/K resulting from the integration of low-temperature heat capacity [ $C_P(T)$ ]  
 460 measurements (Cappelletti et al., 2018), following:

$$461 \quad S_{298}^0 = S_0^0 + \int_0^{298} \left[ \frac{C_P^0(T)}{T} \right] dT \quad (\text{Eq. 14}),$$

462 taking into account that  $S_0^0$ , i.e. the residual entropy at 0 K, is non-zero in amorphous solids;

- 463 • the following parameters were assumed to be the same as for graphite (Holland and Powell,  
 464 1998; Day, 2012), as they have been reported to be very similar in glasslike carbon: i) the  
 465 thermal expansion (cf. Cowland and Lewis, 1967), ii) the coefficients of the heat capacity  
 466 function (cf. Takahashi and Westrum, 1970; Yokoyama et al., 1971) and iii) the standard  
 467 molar volume, relying on the fact that the disordered multilayer graphene component in  
 468 glass-like carbon has a density close to that of graphite ( $2.25 \text{ g/cm}^3$ ) and the interplanar  $d$ -  
 469 spacings are in broad agreement with those of graphite (Supplementary Fig. 3; cf. also Zhao  
 470 et al., 2015; Hu et al., 2017). Models with molar volume increased by 50%, reflecting the  
 471 apparently lower bulk density of glass-like carbon ( $\approx 1.5 \text{ g/cm}^3$ ; Cowland and Lewis, 1967;

472 Zhao et al., 2015) imputable to the high closed porosity, are also provided for comparison in  
473 Figure 7 b–c.

474 • the isothermal bulk modulus under standard conditions ( $K^0$ ) and its first pressure derivative  
475 ( $K'$ ) were retrieved by linear regression of the data of type-I glass-like carbon reported by  
476 Zhao et al. (2015) (green dots in Fig. 7 a), where  $K^0$  is the intercept at 0.0001 GPa (1 bar) at  
477 25°C and  $K'$  is the slope of the  $K$ – $P$  curves. However, the estimation of glass-like carbon  $K^0$   
478 and  $K'$  is not straightforward. Glass-like carbon displays a very high compressibility  
479 compared to graphite (cf. bulk modulus data in Day, 2012; Table 4), with a more than  
480 halved  $K^0$  decreasing abnormally with increasing pressure up to 1 GPa (i.e., negative  $K' = -$   
481 2.4, corresponding to a  $K^0$  intercept of 15 GPa; purple thick dashed lines in Fig. 7), followed  
482 by a reversal to positive pressure dependence, accounting to a  $K'$  of 2.9 in the 1–3 GPa  
483 pressure range (extrapolated  $K^0 = 9$  GPa; red thick lines in Fig. 7; preferred model as it is  
484 consistent with the pressures investigated in this study and with  $K^0$  of other forms of non-  
485 graphitic  $sp^2$ -type carbon; cf. fullerene in Sundqvist and Olabi, 2016) and  $K' = 7.8$  at  
486 pressures above 3 GPa (extrapolated  $K^0 = -6$  GPa; grey dashed lines in Fig. 7). In figure 7b,  
487 we show how the choice of different  $K^0$  and  $K'$  values affects the  $G(P, 800^\circ\text{C})$  of glass-like  
488 carbon with pressure increasing from 0 to 5 GPa. The predicted difference in Gibbs free  
489 energy at 800°C *versus* pressure between glass-like carbon and graphite ( $\Delta G$ ) using the  
490 different models is also shown (Fig. 7c).

491

492 At 800°C, the  $G$ – $P$  curves of glass-like carbon (preferred model) and of graphite cross at 3.4 GPa,  
493 showing a continuous decline of  $\Delta G$  with increasing pressure, which is 1.5 kJ/mol at 1 GPa and  
494 0.29 kJ/mol at 3 GPa. These  $\Delta G$  values match well our experimental results at  $f_{\text{H}_2}^{\text{NNO}}$  conditions  
495 (Table 3). Runs buffered at  $f_{\text{H}_2}^{\text{FMQ}}$  conditions agree with the model at 1 GPa, while at 3 GPa the  
496 decline observed experimentally, characterized by a negative  $\Delta G$ , is more pronounced compared to  
497 the model. Models assuming a molar volume coherent with the apparent bulk density of glass-like  
498 carbon ( $1.5 \text{ g/cm}^3$ ) are inconsistent with experimental results, as they show  $\Delta G$  values that would  
499 increase by increasing pressures (red dashed line in Fig. 7). Negative  $\Delta G$  values at 3 GPa can be  
500 reproduced only by models that assume very high compressibility ( $K^0 = 2$  GPa; orange dashed line  
501 in Figure 7). In this case, however, the intersection point with graphite is shifted at lower pressures  
502 ( $\approx 1.5$  GPa), so that the  $G$ – $P$  curve of glass-like carbon would always lie below that of diamond,  
503 meaning that, above the intersection point, glass-like carbon would be the stable form of carbon  
504 relative graphite and diamond, which is unlikely. On the other hand, the preferred model does  
505 intersect the  $G$ – $P$  curve of diamond, although it occurs at 4.2 GPa, i.e., above the intersection point

506 with graphite at 3.4 GPa and above the graphite–diamond transition at 3.7 GPa, too. This would  
507 imply that in the pressure window 3.4–3.7 glass-like carbon could be more stable than graphite and  
508 between 3.7 and 4.2 it could even be more stable than diamond (yellow field in Figure 7). However,  
509 because of the similar slopes of glass-like carbon- and graphite  $G$ – $P$  curves, small fluctuations in  
510 the chosen  $K^0$  can result in large uncertainties on the position of the intersection point with graphite  
511 relative to the graphite-diamond transition. In fact, a glass-like carbon  $G$ – $P$  curve calculated  
512 assuming  $K^0 = 12$  GPa (red dashed lines in Figure 7) instead of  $K^0 = 9$  GPa (preferred model) would  
513 intersect the  $G$ – $P$  curve of diamond at 3.4 GPa and the  $G$ – $P$  curve of graphite at 4 GPa, implying  
514 metastability of glass-like carbon at any pressure towards both graphite and diamond, without  
515 having a marked effect on the predicted decline of  $\Delta G$  with increasing pressure.

516 The estimated thermodynamic parameters of glass-like carbon allow also the calculation of  $fO_2$ – $T$   
517 phase diagrams at high pressures. In Figure 8, the boundaries C–CO<sub>2</sub> (often referred to as CCO) and  
518 enstatite + magnesite = olivine + C (EMOG) are compared considering crystalline graphite and  
519 glass-like carbon. At 1 GPa, CCO<sub>(glass-like carbon)</sub> and EMOG<sub>(glass-like carbon)</sub> are shifted below  
520 CCO<sub>(graphite)</sub> and EMOG<sub>(graphite)</sub> by 0.08 log  $fO_2$  units. At 3.5 GPa, the possible reversed stability of  
521 glass-like carbon over graphite is shown, with CCO<sub>(glass-like carbon)</sub> and EMOG<sub>(glass-like carbon)</sub> located  
522 above CCO<sub>(graphite)</sub> and EMOG<sub>(graphite)</sub> by 0.01 log  $fO_2$  units. In both cases, the difference of CCO  
523 curves pertaining to the two considered types of carbon is very small in terms of absolute  $fO_2$   
524 values. Nevertheless, as shown by our experimental results, these differences are enough to induce  
525 large variations in the composition of COH fluids interacting with crystalline versus glass-like solid  
526 carbon.

527

#### 528 4.4 Comparison of glass-like carbon and glucose-derived char

529 Char synthesized for 24 h at 1 and 3 GPa, 800°C starting from glucose displays conchoidal  
530 fractures (Fig. 3 c–f) and absence of cleavage, similar to glass-like carbon. Moreover, char and  
531 glass-like carbon show broadly similar Raman spectra (Fig. 4), X-ray diffraction patterns  
532 (Supplementary Fig. 3) and nano-sized crystallite dimensions, supporting our experimental strategy  
533 in which glass-like carbon was chosen as the best analogue for disorganized, poorly crystalline  
534 carbonaceous organic matter. In this study, we observed a marked difference in Raman spectra  
535 acquired for char synthesized in 12-h and 24-h runs performed at 1 GPa and 800°C. In particular,  
536 the graphite  $G'$  peak at about 2700 cm<sup>-1</sup>, well developed in the 12-h run, becomes only hinted in the  
537 24-h run, suggesting that the size of the graphite crystallites decreased with time. This implies, in  
538 agreement with Beyssac et al. (2003), that the structure of char, although somewhat similar to glass-  
539 like carbon, is not stable at high-pressure/high-temperature conditions, and so this type of materials



540 would be not suitable for long experiments at static equilibrium conditions. In this study, however,  
541 we observed transient near-equilibrium conditions between char and aqueous fluids generated by  
542 dehydration of glucose. Ideally, in perfectly closed systems, the thermal decomposition of  
543 anhydrous glucose ( $\text{CH}_2\text{O}$ ) should produce carbon and pure water; however, this has been observed  
544 only in the run performed at 3 GPa and 800°C, containing almost pure water ( $\approx 99$  mol%  $\text{H}_2\text{O}$ ). In  
545 fact, dehydration of glucose at 1 GPa produced  $\text{CH}_4$ -rich,  $\text{CO}_2$ -bearing fluids after 12 h and  $\text{CO}_2$ -  
546 rich,  $\text{CH}_4$ -bearing fluids after 24 h. However, if the measured composition of these fluids is  
547 compared with those predicted by the modified model of Zhang and Duan (2009) implemented with  
548 the retrieved glass-like carbon equilibrium constants, both  $X_{\text{CO}_2}$  and  $X_{\text{CH}_4}$  ratios match redox  
549 conditions of  $\Delta\text{FMQ} = -1.8$ , suggesting near-equilibrium conditions and a close thermodynamic  
550 affinity between glass-like carbon and char. In longer runs (24 h) at the same conditions of 1 GPa  
551 and 800°C, measured  $X_{\text{CO}_2}$  and  $X_{\text{CH}_4}$  ratios correspond also in this case to consistent redox states  
552 ( $\Delta\text{FMQ} = -1.2$ , if  $X_{\text{CO}_2}$  is considered;  $\Delta\text{FMQ} = -1.0$  if  $X_{\text{CH}_4}$  is taken into account). The measured  
553 fluid compositions suggest that the interaction with char in unbuffered single gold capsules evolves  
554 over time from reduced conditions, likely buffered by glucose (Hawkins, 1929; Kunz et al., 2011),  
555 to more oxidized conditions, likely constrained by the MgO–graphite–NaCl–Pyrex furnace  
556 assembly (close to FMQ; cf. Olafsson and Eggler, 1983). In agreement with previous studies (e.g.,  
557 Truckenbrodt et al., 1997; Truckenbrodt and Johannes, 1999; Matjuschkin et al., 2014), we  
558 observed that unbuffered single gold capsules cannot therefore be considered systems perfectly  
559 closed to  $\text{H}_2\text{O}$  and  $\text{H}_2$ , so the buffering of the system (for instance using double capsules) is  
560 mandatory to constrain the  $\text{H}_2$  (and, indirectly, the  $\text{O}_2$ ) chemical potential.

561

#### 562 *4.5 Implications for organic matter dissolution at subduction zones*

563 Organic matter can be an important constituent of oceanic sediments (Mayer et al., 1992), and on  
564 average it accounts for less than 1 wt.% (Kelemen and Manning, 2015). Nevertheless, organic  
565 matter in deep-sea fans can dominate the carbon input flux at some margins (Plank and Manning,  
566 2019). The proportion of organic to inorganic carbon (i.e., marine carbonates) subducted globally is  
567 about 20% (Plank and Manning, 2019) and the total amount of organic carbon subducted in modern  
568 active subduction zones is estimated  $>11$  Mt C/y (Clift, 2017). Once subducted and heated, poorly  
569 organized organic matter is progressively transformed into crystalline graphite through a multitude  
570 of intermediate stages generally referred to disordered graphitic carbon (Beyssac and Rumble,  
571 2014; Buseck and Beyssac, 2014). In addition, graphite can also form by reduction of carbonates  
572 during subduction (Galvez et al., 2013; Vitale-Brovarone et al., 2017) and by precipitation from  
573 subduction C-O-H fluids (Luque et al., 1998).

574

575 The oxidation susceptibility and therefore the dissolution of graphite in aqueous fluids varies as a  
576 function of  $P$ ,  $T$  and  $f\text{O}_2$  conditions (e.g., Connolly, 1995; Tumiati and Malaspina, 2019). In  
577 general, low-temperature and high-pressure conditions characterizing subduction zones are thought  
578 to promote the stability of graphite, thus fluids interacting with this mineral should contain very low  
579 amounts of carbon and are essentially nearly pure water (Schmidt and Poli, 2013). However, we  
580 show in Figure 9 a that this is expected only at forearc conditions. In fact, at  $P$ – $T$  conditions  
581 characterizing the slab surface (Syracuse et al., 2010), nearly pure water is expected only up to  
582 around 2 GPa and 450°C. At greater depths, graphite-saturated fluids become progressively more  
583 enriched in  $\text{CO}_2$  as FMQ and CCO buffers get very close (Fig. 9 a), with maximum  $\text{CO}_2$  contents  
584 ( $X_{\text{CO}_2} = 0.55$ ) at subarc conditions (3 GPa–700°C), where the two buffers nearly converge. These  
585 fluid compositions are predicted assuming a perfectly crystalline and ordered state of graphite.  
586 Several previous studies suggested that the poorly ordered graphite might behave differently, in  
587 particular showing a higher solubility in aqueous fluids (Ziegenbein and Johannes, 1980; Connolly,  
588 1995; Luque et al., 1998). Although our investigated  $P$ – $T$  conditions are not strictly comparable  
589 with "normal" subduction regimes, especially at low pressures, we demonstrate that glass-like  
590 carbon is characterized by a marked difference in free energy ( $\approx 2$  kJ/mol) with respect to  
591 crystalline graphite at low pressures, diminishing with increasing pressures and with a possible sign  
592 reversal close to graphite-diamond transition (located at 3.6 GPa and 760°C in Fig. 9 a). Because  
593 we showed that the difference in free energy between graphite and glass-like carbon is  
594 predominantly due to their different compressibility behavior, the relative difference in carbon  
595 solubility is only slightly depending on temperature. Therefore, we can speculate that similar  
596 differences in fluid carbon content (in terms of  $\text{CO}_{2(\text{aq})}$ , but possibly also of  $\text{CH}_{4(\text{aq})}$ ,  $\text{HCO}_3^-$ ,  $\text{CO}_3^{2-}$   
597 and other dissolved C–O–H species at appropriate  $P$ – $T$ – $f\text{O}_2$ – $f\text{H}_2$ –pH conditions) can be expected at  
598 lower temperatures characterizing the subduction zones and in particular the subduction surface  
599 where sediments containing organic matter can be abundant.

600 This implies that disordered graphitic carbon is more prone to oxidation if compared with ordered  
601 crystalline graphite down to about 110 km, resulting in fluids that are enriched in  $\text{CO}_2$  compared to  
602 current estimates: the lower the pressure the higher the differential dissolution susceptibility.  
603 Therefore, because it is unlikely that organic carbon can persist in its disordered state at great  
604 depths and consequent relatively high temperatures (Beyssac et al., 2002), and because the  
605 difference in free energy is higher at low pressures, we infer that the most important effect on  
606 carbon recycling concerns the most shallow levels of subduction zones, where disordered organic  
607 carbon could be far more reactive than expected for graphite towards aqueous fluids (Fig. 9 b).

608 Obviously an important source of uncertainty arises from the assumption that glass-like carbon can  
609 be considered an analogue of disordered natural carbonaceous matter. Carbon materials are very  
610 complex because their properties change extensively with structural defects and impurities, and the  
611 type of hybridization, in particular  $sp^2$  (graphite-like carbon) vs.  $sp^3$  (diamond-like carbon) (e.g.,  
612 Robertson, 2002; Langenhorst and Campione, 2019). Moreover, the activity and the reactivity of  
613 these materials can be modified by bringing them to nanosize dimensions. For instance, Guencheva  
614 et al. (2001) and Gutzow et al. (2005) showed that nanodispersed (10 nm) glass-like carbon displays  
615 a difference in Gibbs free energy compared to graphite of +12 kJ/mol at standard conditions, which  
616 is substantially higher relative to bulk glass-like carbon (+2.4 kJ/mol; Table 4) and which would  
617 result in dissolution susceptibility higher than that provided in our study. In addition, natural highly  
618 disordered carbon, as synthetic amorphous and graphitic carbon, is likely characterized by a higher  
619 kinetic reactivity because of the presence of active immobilized free radicals (dangling bonds) and  
620 defects which make these materials efficient catalysts (e.g., Jüntgen, 1986). The results provided in  
621 our study therefore represent a first attempt to provide a conservative minimum estimate of the  
622 enhanced dissolution of disordered carbon with respect to crystalline graphite in natural systems.

623

## 624 **5. Conclusions**

625 Well-ordered crystalline graphite and X-ray amorphous glass-like carbon display different  
626 dissolution susceptibility in aqueous fluids, because of their different thermodynamic properties. On  
627 the basis of our experimental observations concerning this type of disordered  $sp^2$  carbon, and aware  
628 of the uncertainties arising from the choice of glass-like carbon as an analogue materials for  
629 naturally occurring poorly organized carbon derived from the graphitization of organic matter, we  
630 may speculate at this stage that also natural poorly organized graphitic carbon could behave in a  
631 different manner compared to perfectly crystalline graphite. In particular, disordered carbonaceous  
632 matter could be more prone to dissolve in aqueous fluids compared to well-crystallized graphite  
633 especially at pressures corresponding to the forearc region of subduction zones. High fluxes of  
634 water coming from the dehydration of the down-going slab would therefore induce an effective  
635 removal of organic matter from its sedimentary cover, prompting metasomatism of the mantle  
636 wedge (Sieber et al., 2018) and contributing to the global deep carbon cycle. As for glass-like  
637 carbon, the differential dissolution susceptibility declines with increasing pressure corresponding to  
638 110 km depth, below which "disordered" carbon could be even less soluble than graphite. The  
639 stability of glass-like carbon over diamond, although predicted by the suggested model in the 3.7–  
640 4.2 GPa pressure window, relies on thermodynamic parameters that are affected by uncertainties  
641 that are currently unquantifiable. The occurrence of nano-crystalline disordered graphitic carbon

642 and amorphous  $sp^2$  and  $sp^3$  carbon has been indeed reported in micro- and nano-sized diamonds  
643 from Cignana Lake in the Western Alps (Frezzotti et al., 2014; Frezzotti, 2019) and glass-like X-ray  
644 amorphous carbon has been obtained experimentally at diamond-stable conditions (7.7 GPa and  
645 1000°C; Yamaoka et al., 2002). However, more investigations are required to confirm this  
646 hypothesis.

647

#### 648 **Appendix: terminology used for the description of solid carbon**

649 In this study, the terminology used for the description of solid carbon follows the recommendations  
650 of IUPAC (Fitzer et al., 1995).

- 651 • Graphite: an allotropic form of the element carbon consisting of layers of hexagonally  
652 arranged carbon atoms in a planar condensed ring system (graphene layers). The layers are  
653 stacked parallel to each other in a three-dimensional crystalline long-range order. The  
654 chemical bonds within the layers are covalent with  $sp^2$  hybridization.
- 655 • Graphitic carbon: all varieties of substances consisting of the element carbon in the  
656 allotropic form of graphite irrespective of the presence of structural defects. The use of the  
657 term is justified if three-dimensional hexagonal long-range order can be detected in the  
658 material by diffraction methods, independent of the volume fraction and the homogeneity of  
659 distribution of such crystalline domains.
- 660 • Glass-like carbon: in this study we use this term although the commercial/trademark terms  
661 "glassy carbon" and "vitreous carbon" are still widely used in experimental petrology and  
662 materials sciences papers. Glass-like carbon is a granular (i.e., homogenous microstructure  
663 with structural elements undistinguishable by optical microscopy) and non-graphitizable  
664 carbon (i.e., it does not convert into graphitic carbon upon heat treatment to 2500–3300 K)  
665 with a very high isotropy. Although its structure is not comparable to silicate glasses, the  
666 fracture surfaces have a pseudo-glassy (conchoidal) appearance. It consists of curved two-  
667 dimensional structural elements (graphene layers, i.e., single carbon layers of the graphite  
668 structure) dispersed in an X-ray amorphous matrix, but it does not exhibit dangling bonds  
669 that characterize the so-called "amorphous carbon". In fact, the term "amorphous carbon" is  
670 restricted to the description of carbon materials which, in addition to a lack of long-range  
671 crystalline order and to deviations of the interatomic distances with respect to graphite  
672 lattice as well as to the diamond lattice, show deviations in the bond angles because of the  
673 presence of dangling bonds. Amorphous carbon is disordered even on the atomic scale and  
674 have a fraction of  $sp^3$  bonds ranging from a few ("graphite-like" structure) to almost 100%  
675 ("diamond-like" structure) (Sundqvist and Olabi, 2016)

676 • Char: a solid decomposition product of a natural or synthetic organic material. In this study,  
677 char is produced by carbonization (pyrolysis) of glucose. The term pyrolytic carbon has  
678 been avoided because it is restricted to carbon materials deposited from gaseous  
679 hydrocarbon compounds by chemical vapor deposition.  
680

## 681 **Acknowledgements**

682 Luca Toffolo is acknowledged for preliminary Raman analyses, Andrea Risplendente for help at the  
683 microprobe, and Andrea Amalfa for preparing some of the experiments. Alberto Villa is thanked for  
684 helpful discussions about synthetic carbon forms. Elettra is acknowledged for synchrotron  
685 beamtime. Maurizio Polentarutti and Marco Merlini for help at the synchrotron. The authors are  
686 indebted to the reviewers Yuan Li and Matt Steele-MacInnis for their useful suggestions.  
687 Suggestions by the Associate Editor Rajdeep Dasgupta also contributed to a significant  
688 improvement of the paper.  
689

## 690 **Funding:**

691 ST and SP acknowledge support from Deep Carbon Observatory - Sloan Foundation and from  
692 Italian program MIUR PRIN 2017ZE49E7\_002. AVB acknowledges funding from the *Agence*  
693 *Nationale des Recherches* (ANR; grant T-ERC), France, and from the Levi Montalcini program by  
694 MIUR, Italy. CEM acknowledges support from US National Science Foundation grant EAR  
695 1732256.  
696

## 697 **References**

698 Bernard S., Benzerara K., Beyssac O., Menguy N., Guyot F., Brown G. E. and Goffé B. (2007)  
699 Exceptional preservation of fossil plant spores in high-pressure metamorphic rocks. *Earth*  
700 *Planet. Sci. Lett.* **262**, 257–272.

701 Beyssac O., Brunet F., Petitet J.-P., Goffé B. and Rouzaud J.-N. (2003) Experimental study of the  
702 microtextural and structural transformations of carbonaceous materials under pressure and  
703 temperature. *Eur. J. Mineral.* **15**, 937–951. Available at:  
704 [http://www.ingentaselect.com/rpsv/cgi-bin/cgi?ini=xref&body=linker&reqdoi=10.1127/0935-](http://www.ingentaselect.com/rpsv/cgi-bin/cgi?ini=xref&body=linker&reqdoi=10.1127/0935-1221/2003/0015-0937)  
705 [1221/2003/0015-0937](http://www.ingentaselect.com/rpsv/cgi-bin/cgi?ini=xref&body=linker&reqdoi=10.1127/0935-1221/2003/0015-0937).

706 Beyssac O., Rouzaud J.-N., Goffé B., Brunet F. and Chopin C. (2002) Graphitization in a high-  
707 pressure, low-temperature metamorphic gradient: a Raman microspectroscopy and HRTEM  
708 study. *Contrib. to Mineral. Petrol.* **143**, 19–31. Available at:  
709 <http://link.springer.com/10.1007/s00410-001-0324-7>.

710 Beyssac O. and Rumble D. (2014) Graphitic carbon: A ubiquitous, diverse, and useful geomaterial.  
711 *Elements* **10**, 415–420.

712 Bollinger L., Avouac J. P., Beyssac O., Catlos E. J., Harrison T. M., Grove M., Goffé B. and  
713 Sapkota S. (2004) Thermal structure and exhumation history of the Lesser Himalaya in central  
714 Nepal. *Tectonics* **23**, 1–19.

715 Bose K. and Ganguly J. (1995) Quartz-coesite transition revisited - Reversed experimental determi  
716 at 500-1200 °C and retrieved thermochemical properties. *Am. Mineral. Mineral.* **80**, 231–238.

717 Buseck P. R. and Beyssac O. (2014) From organic matter to graphite: Graphitization. *Elements* **10**,  
718 421–426.

719 Cappelletti R. L., Udovic T. J. and Paul R. L. (2018) Glassy carbon , NIST Standard Reference  
720 Material (SRM 3600): hydrogen content , neutron vibrational density of states and heat  
721 capacity. *J. Appl. Crystallogr.* **51**, 1323–1328.

722 Cartigny P., Stachel T., Harris J. W. and Javoy M. (2004) Constraining diamond metasomatic  
723 growth using C- and N-stable isotopes: Examples from Namibia. *Lithos* **77**, 359–373.

724 Clift P. D. (2017) A revised budget for Cenozoic sedimentary carbon subduction. *Rev. Geophys.* **55**,  
725 97–125.

726 Connolly J. A. D. (2005) Computation of phase equilibria by linear programming: A tool for  
727 geodynamic modeling and its application to subduction zone decarbonation. *Earth Planet. Sci.*  
728 *Lett.* **236**, 524–541.

729 Connolly J. A. D. (1995) Phase diagram methods for graphitic rocks and application to the system. ,  
730 94–116.

731 Connolly J. A. D. and Cesare B. (1993) C-O-H-S fluid composition and oxygen fugacity in  
732 graphitic metapelites. *J. Metamorph. Geol.* **11**, 379–388.

733 Cowlard F. C. and Lewis J. C. (1967) Vitreous Carbon - A New Form of Carbon. *J. Mater. Sci.* **2**,  
734 507–512.

735 Dasgupta R., Hirschmann M. M. and Dellas N. (2005) The effect of bulk composition on the  
736 solidus of carbonated eclogite from partial melting experiments at 3 GPa. *Contrib. to Mineral.*  
737 *Petrol.* **149**, 288–305.

738 Day H. W. (2012) A revised diamond-graphite transition curve. *Am. Mineral.* **97**, 52–62.

739 Duncan M. S. and Dasgupta R. (2017) Rise of Earth's atmospheric oxygen controlled by efficient  
740 subduction of organic carbon. *Nat. Geosci.* **10**, 387–392.

741 Eugster H. P. and Skippen G. B. (1967) Igneous and metamorphic reactions involving gas  
742 equilibria. *Res. Geochemistry* **2**, 492–520.

743 Falloon T. J., Green D. H., Danyushevsky L. V. and McNeill A. W. (2008) The composition of

744 near-solidus partial melts of fertile peridotite at 1 and 1.5 GPa: Implications for the  
745 petrogenesis of MORB. *J. Petrol.* **49**, 591–613.

746 Ferrari A. C. (2007) Raman spectroscopy of graphene and graphite: Disorder, electron-phonon  
747 coupling, doping and nonadiabatic effects. *Solid State Commun.* **143**, 47–57.

748 Ferrari A. C. and Robertson J. (2001) Resonant Raman spectroscopy of disordered, amorphous, and  
749 diamond-like carbon. *Phys. Rev. B* **64**, 075414.

750 Fitzer E., Köchling K. H., Boehm H. P. and Marsh H. (1995) Recommended terminology for the  
751 description of carbon as a solid. *Pure Appl. Chem.* **67**, 473–506.

752 Frezzotti M. L. (2019) Diamond growth from organic compounds in hydrous fluids deep within the  
753 Earth. *Nat. Commun.* **10**. Available at: <http://dx.doi.org/10.1038/s41467-019-12984-y>.

754 Galvez M. E., Beyssac O., Martinez I., Benzerara K., Chaduteau C., Malvoisin B. and Malavieille J.  
755 (2013) Graphite formation by carbonate reduction during subduction. *Nat. Geosci.* **6**, 473–477.  
756 Available at: <http://dx.doi.org/10.1038/ngeo1827>.

757 Guencheva V., Grantscharova E. and Gutzow I. (2001) Thermodynamic properties of the  
758 amorphous and crystalline modifications of carbon and the metastable synthesis of diamond.  
759 *Cryst. Res. Technol.* **36**, 1411–1428.

760 Gutzow I., Todorova S., Kostadinov L., Stoyanov E., Guencheva V., Völksch G., Dunken H. and  
761 Rüssel C. (2005) Diamonds by transport reactions with vitreous carbon and from the plasma  
762 torch: new and old methods of metastable diamond syhtnesis and growth. In *Nucleation theory  
763 and applications (Schmelzer, J. W. P., ed.)* (ed. J. W. P. Schmelzer). Wiley-VCH Verlag. pp.  
764 256–311.

765 Hawkins J. A. (1929) Reducing powers of different sugars for the ferricyanide reagent used in the  
766 gasometric sugar method. *J. Biol. Chem.* **84**, 79–83.

767 Hayes J. M. and Waldbauer J. R. (2006) The carbon cycle and associated redox processes through  
768 time. *Philos. Trans. R. Soc. Lond. B. Biol. Sci.* **361**, 931–950.

769 Holland T. J. B. and Powell R. (1998) An internally consistent thermodynamic data set for phases  
770 pf petrological interest. *J. Metamorph. Geol.* **16**, 309–343.

771 Hu M., He J., Zhao Z., Strobel T. A., Hu W., Yu D., Sun H., Liu L., Li Z., Ma M., Kono Y., Shu J.,  
772 Mao H., Fei Y., Shen G., Wang Y., Juhl S. J., Huang J. Y., Liu Z., Xu B. and Tian Y. (2017)  
773 Compressed glassy carbon : An ultrastrong and elastic interpenetrating graphene network. *Sci.  
774 Adv.* **3**, e1603213.

775 Huang F., Daniel I., Cardon H., Montagnac G. and Sverjensky Di. A. (2017) Immiscible  
776 hydrocarbon fluids in the deep carbon cycle. *Nat. Commun.* **8**, 15798.

777 Huang F. and Sverjensky D. A. (2019) Extended Deep Earth Water Model for predicting major

778 element mantle metasomatism. *Geochim. Cosmochim. Acta* **254**, 192–230. Available at:  
779 <https://doi.org/10.1016/j.gca.2019.03.027>.

780 Jüntgen H. (1986) Activated carbon as catalyst support. A review of new research results. *FUEL* **65**,  
781 1436–1446.

782 Kelemen P. B. and Manning C. E. (2015) Reevaluating carbon fluxes in subduction zones, what  
783 goes down, mostly comes up. *Proc. Natl. Acad. Sci.*, 201507889. Available at:  
784 <http://www.pnas.org/lookup/doi/10.1073/pnas.1507889112>.

785 Kunz T., Lee E. J., Schiwiek V., Seewald T. and Methner F. J. (2011) Glucose - A reducing sugar?  
786 Reducing properties of sugars in beverages and food. *BrewingScience* **64**, 61–67.

787 Langenhorst F. and Campione M. (2019) Ideal and real structures of different forms of carbon, with  
788 some remarks on their geological significance. *J. Geol. Soc. London*. **176**, 337–347.

789 Li Y. (2016) T1 - Immiscible C-H-O fluids formed at subduction zone conditions. *Geochemical*  
790 *Perspect. Lett.* **3**, 12–21. Available at:  
791 <http://www.geochemicalperspectivesletters.org/article1702>.

792 Luque F. J., Pasteris J. D., Wopenka B., Rodas M. and Barrenechea J. F. (1998) Natural fluid-  
793 deposited graphite: Mineralogical characteristics and mechanisms of formation. *Am. J. Sci.*  
794 **298**, 471–498.

795 Luth R. W. (1989) Natural versus experimental control of oxidation state : Effects on the  
796 composition and speciation of C-O-H fluids. *Am. Mineral.* **74**, 50–57.

797 Manning C. E., Shock E. L. and Sverjensky D. A. (2013) The chemistry of carbon in aqueous fluids  
798 at crustal and upper-mantle conditions: experimental and theoretical constraints. *Rev. Mineral.*  
799 *Geochemistry* **75**, 109–148. Available at:  
800 <https://pubs.geoscienceworld.org/rimg/article/75/1/109-148/140933> [Accessed April 5, 2019].

801 Mason E., Edmonds M. and Turchyn A. V (2017) Remobilization of crustal carbon may dominate  
802 volcanic arc emissions. *Science (80-. )*. **357**, 290–294.

803 Matjuschkin V., Brooker R. A., Tattitch B., Blundy J. D. and Stamper C. C. (2014) Control and  
804 monitoring of oxygen fugacity in piston cylinder experiments. *Contrib. to Mineral. Petrol.*  
805 **169**, 1–16.

806 Mattioli G. S. and Wood B. J. (1988) Magnetite activities across the MgAl<sub>2</sub>O<sub>4</sub>-Fe<sub>3</sub>O<sub>4</sub> spinel join,  
807 with application to thermobarometric estimates of upper mantle oxygen fugacity. *Contrib. to*  
808 *Mineral. Petrol.* **98**, 148–162.

809 Matveev S., Ballhaus C., Fricke K., Truckenbrodt J. and Ziegenben D. (1997) Volatiles in the  
810 Earth's mantle: I. Synthesis of CHO fluids at 1273 K and 2.4 GPa. *Geochim. Cosmochim. Acta*  
811 **61**, 3081–3088.



812 Mayer L., Piasias N. and Janacek T. (1992) 14. SITE 849. *Proc. Ocean Drill. Program. Initial*  
813 *reports*. **138**, 735–807.

814 McCollom T. M. (2013) Laboratory simulations of abiotic hydrocarbon formation in Earth's deep  
815 subsurface. *Rev. Mineral. Geochemistry* **75**, 467–494. Available at:  
816 <http://ring.geoscienceworld.org/cgi/doi/10.2138/rmg.2013.75.15>.

817 O'Neill H. S. C. and Pownceby M. I. (1993) Thermodynamic data from redox reactions at high  
818 temperatures. I. An experimental and theoretical assessment of the electrochemical method  
819 using stabilized zirconia electrolytes, with revised values for the Fe-"FeO", Co-CoO, Ni-NiO  
820 and Cu-Cu<sub>2</sub>O oxygen buffers, and new data for the W-WO<sub>2</sub> buffer. *Contrib. to Mineral.*  
821 *Petrol.* **114**, 296–314. Available at: <http://link.springer.com/article/10.1007/BF01046533>.

822 Olafsson M. and Eggler D. H. (1983) Phase relations of amphibole, amphibole-carbonate, and  
823 phlogopite-carbonate peridotite: petrologic constraints on the asthenosphere. *Earth Planet. Sci.*  
824 *Lett.* **64**, 305–315.

825 Palot M., Pearson D. G., Stern R. A., Stachel T. and Harris J. W. (2014) Isotopic constraints on the  
826 nature and circulation of deep mantle C-H-O-N fluids: Carbon and nitrogen systematics within  
827 ultra-deep diamonds from Kankan (Guinea). *Geochim. Cosmochim. Acta* **139**, 26–46.  
828 Available at: <http://dx.doi.org/10.1016/j.gca.2014.04.027>.

829 Pan D. and Galli G. (2016) The fate of carbon dioxide in water-rich fluids under extreme  
830 conditions. *Sci. Adv.* **2**, e1601278. Available at:  
831 <http://advances.sciencemag.org/cgi/doi/10.1126/sciadv.1601278>.

832 Plank T. and Manning C. E. (2019) Subducting carbon. *Nature* **574**, 343–352. Available at:  
833 <http://dx.doi.org/10.1038/s41586-019-1643-z>.

834 Ponschke M. A. and House J. E. (2011) Kinetic studies on the loss of water from  $\alpha$ -D-glucose  
835 monohydrate. *Carbohydr. Res.* **346**, 2285–2289. Available at:  
836 <http://dx.doi.org/10.1016/j.carres.2011.07.012>.

837 Robertson J. (2002) Diamond-like amorphous carbon. *Mater. Sci. Eng. Reports* **37**, 129–281.

838 Robinson J. A. C., Wood B. J. and Blundy J. D. (1998) The beginning of melting of fertile and  
839 depleted peridotite at 1.5 GPa. *Earth Planet. Sci. Lett.* **155**, 97–111.

840 Schmidt M. W. and Poli S. (2013) Devolatilization during subduction. *Treatise Geochemistry 2nd*  
841 *Ed.* **4**, 669–701. Available at: <http://dx.doi.org/10.1016/B978-0-08-095975-7.00321-1>.

842 Shiell T. B., McCulloch D. G., McKenzie D. R., Field M. R., Haberl B., Boehler R., Cook B. A.,  
843 De Tomas C., Suarez-Martinez I., Marks N. A. and Bradby J. E. (2018) Graphitization of  
844 glassy carbon after compression at room temperature. *Phys. Rev. Lett.* **120**, 215701. Available  
845 at: <https://doi.org/10.1103/PhysRevLett.120.215701>.

- 846 Sieber M. J., Hermann J. and Yaxley G. M. (2018) An experimental investigation of C–O–H fluid-  
847 driven carbonation of serpentinites under forearc conditions. *Earth Planet. Sci. Lett.* **496**, 178–  
848 188. Available at: <https://doi.org/10.1016/j.epsl.2018.05.027>.
- 849 Spandler C., Yaxley G., Green D. H. and Rosenthal A. (2008) Phase relations and melting of  
850 anhydrous K-bearing eclogite from 1200 to 1600°C and 3 to 5 GPa. *J. Petrol.* **49**, 771–795.
- 851 Stachel T., Harris J., Aulbach S. and Deines P. (2002) Kankan diamonds (Guinea) III:  $\delta^{13}\text{C}$  and  
852 nitrogen characteristics of deep diamonds. *Contrib. to Mineral. Petrol.* **142**, 465–475.
- 853 Sundqvist B. and Olabi A. G. (2016) Fullerites and hard carbons. *Ref. Modul. Mater. Sci. Mater.*  
854 *Eng.*
- 855 Sverjensky D. A., Harrison B. and Azzolini D. (2014) Water in the deep Earth: The dielectric  
856 constant and the solubilities of quartz and corundum to 60kb and 1200°C. *Geochim.*  
857 *Cosmochim. Acta* **129**, 125–145. Available at:  
858 <http://linkinghub.elsevier.com/retrieve/pii/S0016703713007151>.
- 859 Sverjensky D. A., Stagno V. and Huang F. (2014) Important role for organic carbon in subduction-  
860 zone fluids in the deep carbon cycle. *Nat. Geosci.* **7**, 909–913. Available at:  
861 <http://www.nature.com/doi/10.1038/ngeo2291>.
- 862 Syracuse E. M., van Keken P. E., Abers G. a., Suetsugu D., Bina C., Inoue T., Wiens D. and  
863 Jellinek M. (2010) The global range of subduction zone thermal models. *Phys. Earth Planet.*  
864 *Inter.* **183**, 73–90.
- 865 Takahashi Y. and Westrum E. F. J. (1970) Glassy carbon low-temperature thermodynamic  
866 properties. *J. Chem. Thermodyn.* **2**, 847–854.
- 867 Tiraboschi Carla, Tumiati S., Recchia S., Miozzi F. and Poli S. (2016) Quantitative analysis of  
868 COH fluids synthesized at HP-HT conditions: an optimized methodology to measure volatiles  
869 in experimental capsules. *Geofluids* **16**, 841–855. Available at:  
870 <http://doi.wiley.com/10.1111/gfl.12191>.
- 871 Tiraboschi C., Tumiati S., Sverjensky D., Pettke T., Ulmer P. and Poli S. (2018) Experimental  
872 determination of magnesia and silica solubilities in graphite-saturated and redox-buffered  
873 high-pressure COH fluids in equilibrium with forsterite + enstatite and magnesite + enstatite.  
874 *Contrib. to Mineral. Petrol.* **173**, 2. Available at: [http://link.springer.com/10.1007/s00410-017-](http://link.springer.com/10.1007/s00410-017-1427-0)  
875 [1427-0](http://link.springer.com/10.1007/s00410-017-1427-0).
- 876 Truckenbrodt J. and Johannes W. (1999) H<sub>2</sub>O loss during piston-cylinder experiments. *Am.*  
877 *Mineral.* **84**, 1333–1335.
- 878 Truckenbrodt J., Ziegenbein D. and Johannes W. (1997) Redox conditions in piston cylinder  
879 apparatus: The different behavior of boron nitride and unfired pyrophyllite assemblies. *Am.*

880 *Mineral.* **82**, 337–344.

881 Tumiati S. and Malaspina N. (2019) Redox processes and the role of carbon-bearing volatiles from  
882 the slab–mantle interface to the mantle wedge. *J. Geol. Soc. London.* **176**, 388–397. Available  
883 at: <http://jgs.lyellcollection.org/lookup/doi/10.1144/jgs2018-046>.

884 Tumiati S., Tiraboschi C., Sverjensky D. A., Pettke T., Recchia S., Ulmer P., Miozzi F. and Poli S.  
885 (2017) Silicate dissolution boosts the CO<sub>2</sub> concentrations in subduction fluids. *Nat. Commun.*  
886 **8**, 616.

887 Vitale Brovarone A., Martinez I., Elmaleh A., Compagnoni R., Chaduteau C., Ferraris C. and  
888 Esteve I. (2017) Massive production of abiotic methane during subduction evidenced in  
889 metamorphosed ophicarbonates from the Italian Alps. *Nat. Commun.* **8**, 14134. Available at:  
890 <http://www.nature.com/doi/10.1038/ncomms14134>.

891 Wasylenki L. E. (2003) Near-solidus Melting of the Shallow Upper Mantle: Partial Melting  
892 Experiments on Depleted Peridotite. *J. Petrol.* **44**, 1163–1191.

893 Yokoyama J., Murabayashi M., Takahashi Y. and Mukaibo T. (1971) Measurement of high-  
894 temperature thermal properties of glassy carbon by laser flash method. *TANSO (in Japanese)*  
895 **1971**, 44–47. Available at:  
896 <http://joi.jlc.jst.go.jp/JST.Journalarchive/tanso1949/1971.44?from=CrossRef> [Accessed  
897 January 29, 2019].

898 Zhang C. and Duan Z. (2009) A model for C-O-H fluid in the Earth's mantle. *Geochim.*  
899 *Cosmochim. Acta* **73**, 2089–2102. Available at: <http://dx.doi.org/10.1016/j.gca.2009.01.021>.

900 Zhang C. and Duan Z. (2010) GFluid: An Excel spreadsheet for investigating C–O–H fluid  
901 composition under high temperatures and pressures. *Comput. Geosci.* **36**, 569–572. Available  
902 at: <http://linkinghub.elsevier.com/retrieve/pii/S0098300409002751>.

903 Zhang S., Ague J. J. and Vitale Brovarone A. (2018) Degassing of organic carbon during regional  
904 metamorphism of pelites, Wepawaug Schist, Connecticut, USA. *Chem. Geol.* **490**, 30–44.  
905 Available at: <https://doi.org/10.1016/j.chemgeo.2018.05.003>.

906 Zhao Z., Wang E. F., Yan H., Kono Y., Wen B., Bai L., Shi F., Zhang J., Kenney-Benson C., Park  
907 C., Wang Y. and Shen G. (2015) Nanoarchitected materials composed of fullerene-like  
908 spheroids and disordered graphene layers with tunable mechanical properties. *Nat. Commun.* **6**,  
909 1–10. Available at: <http://dx.doi.org/10.1038/ncomms7212>.

910 Ziegenbein D. and Johannes W. (1980) Graphite in C-H-O fluids: An unsuitable compound to  
911 buffer fluid composition at temperatures up to 700°C. *Neues Jahrb. für Mineral. Monatshefte*  
912 **7**, 289–305.

913

914 **Tables**

915 Table 1: Run table of the experiments and volatiles measured using the capsule-piercing technique.

916 Table 2: Thermodynamic modeling of graphite-saturated fluids buffered at the investigated  $P$ – $T$ –  
917  $fH_2$  conditions.

918 Table 3: Equilibrium constants ( $K_p$ ) and difference in Gibbs free energy of glassy carbon with  
919 respect to crystalline graphite ( $\Delta G$ ), retrieved from measured fluid composition.

920 Table 4: Thermodynamic properties of graphite and glass carbon (preferred model) at different  
921 pressures and temperatures. See also Supplementary Table 1 for Perple\_X formatted version  
922 including diamond.

923

924 **Figure captions:**

925 Figure 1: Experimental setup. (A, B): sketch of the double capsule system. The inner Au–Pd  
926 capsule, permeable to  $H_2$ , contains oxalic acid dihydrate (OAD), which decomposes at  $T > 200^\circ\text{C}$   
927 to  $CO_2$ ,  $H_2O$  and  $H_2$ , and either crystalline graphite (A) of glass-like carbon (B). The outer Au  
928 capsule contains the inner capsule and the  $fH_2$  buffer, either fayalite-magnetite-quartz- $H_2O$  or  
929 nickel-nickel-oxide- $H_2O$ . The  $fH_2$  constrained by the buffer is expected to be homogenous in the  
930 inner and in the outer capsule. (C): back-scattered electron image of the representative sample  
931 COH62 ( $P = 1$  GPa and  $T = 800^\circ\text{C}$ ) across the inner Au–Pd capsule boundary, showing glass-like  
932 carbon spheres on the left and the fayalite-magnetite-quartz buffer on the right.

933 Figure 2: Micro-Raman spectra of glass-like carbon as starting material (unpolished: blue; polished:  
934 purple) and as quenched product from 1 GPa– $800^\circ\text{C}$  (green) and from 3 GPa– $800^\circ\text{C}$  (red).

935 Figure 3: Secondary electron images of char synthesized from glucose at  $800^\circ\text{C}$  and high-pressure  
936 conditions. (A, B):  $P = 1$  GPa, runtime 12 h; (C, D):  $P = 1$  GPa, runtime 24 h; (E, F):  $P = 3$  GPa,  
937 runtime 24 h.

938 Figure 4: Raman spectra of quenched char (1 GPa: blue; 3 GPa: purple) compared with glass-like  
939 carbon (green) and crystalline graphite (red).

940 Figure 5: Fluid compositions at the investigated  $P$ – $T$ – $fH_2$  measured by using the capsule-piercing  
941 technique (C. Tiraboschi et al., 2016), plotted on ternary C–O–H diagrams. Green triangles: fluids  
942 in equilibrium with crystalline graphite. Blue dots: fluids in equilibrium with glass-like carbon.  
943 Yellow squares: composition of graphite-saturated fluids according to the modified model of Zhang  
944 and Duan (2009) (see text for details). Grey dots: analytical uncertainty cloud estimated by Monte  
945 Carlo method using the standard deviations provided in Table 1.

946 Figure 6:  $\log f_{\text{O}_2}$  vs pH diagrams at 1 GPa–800°C (A) and 3 GPa–800°C (B), calculated using the  
947 Deep Earth Water model, showing the COH-fluid graphite saturation curve (thick black). Black  
948 dots: experimental conditions at  $f_{\text{H}_2}^{\text{FMQ}}$  and  $f_{\text{H}_2}^{\text{NNO}}$ .

949 Figure 7: Thermodynamic properties of glass-like carbon. (A) glass-like carbon bulk modulus and  
950 its pressure dependence, compared with graphite. Measurements from Zhao et al. (2015) (green  
951 dots) are fitted with different  $K^0$  and  $K'$ . The preferred model (red thick) assumes  $K^0 = 9$  GPa and  $K'$   
952 = 2.9. See text for other details. (B) Gibbs free energy versus pressure at 800°C, calculated using  
953 different thermodynamic models of glassy carbon. Red arrows indicate the shift of the preferred  
954 model assuming either an increased molar volume (i.e., lower density) or an increased  
955 compressibility (lower  $K^0$ ). (C) difference in Gibbs free energy between glass-like carbon and  
956 graphite ( $\Delta G$ ), plotted as a function of pressure at  $T = 800^\circ\text{C}$ . Red thick (preferred model):  $K^0 = 9$   
957 GPa,  $K' = 2.9$ , density ( $d$ ) = 2.2.5 g/cm<sup>3</sup>. Red dashed:  $K^0 = 12$  GPa,  $K' = 2.9$ ,  $d = 2.25$  g/cm<sup>3</sup>. Purple  
958 dashed:  $K^0 = 15$  GPa,  $K' = -2.4$ ,  $d = 2.25$  g/cm<sup>3</sup>. Orange dashed:  $K^0 = 0.1$  GPa,  $K' = 6.3$ ,  $d = 2.25$   
959 g/cm<sup>3</sup>. Green dashed:  $K^0 = 9$  GPa,  $K' = 2.9$ ,  $d = 1.5$  g/cm<sup>3</sup>. Blue: diamond. Black thick: graphite.  
960 Light yellow field: thermodynamic stability of glass-like carbon (preferred model) over graphite  
961 and diamond.

962 Figure 8: Calculated  $T$ – $\log f_{\text{O}_2}$  diagrams of the univariant equilibria  $\text{C} + \text{O}_2 = \text{CO}_2$  (CCO) and  
963  $\text{MgSiO}_3 + \text{MgCO}_3 = \text{Mg}_2\text{SiO}_4 + \text{C} + \text{O}_2$  (EMOG) involving graphite and glass-like carbon close to  
964  $T = 800^\circ\text{C}$  at  $P = 1$  GPa and at  $P = 3.5$  GPa, using the thermodynamic properties reported in Table  
965 4. FMQ: fayalite–magnetite–quartz or ferrosilite (fs)–magnetite (mt)–coesite (coes) oxygen buffer.

966 Figure 9: Fate of organic matter in subduction. (A) Stability of COH fluids (grey field) calculated as  
967 a function of  $f_{\text{O}_2}$  along a subduction  $P$ – $T$  gradient consistent with the average thermal model of slab  
968 surface after Syracuse et al. (2010). COH fluids are stable between the two boundaries  $\text{C} + \text{O}_2 =$   
969  $\text{CO}_2$  (CCO) and  $\text{C} + 2 \text{H}_2 = \text{CH}_4$ . At this scale, differences between graphite and amorphous carbon  
970 are negligible, but according to the preferred model in Figure 7 glass-like carbon would be the  
971 stable carbon polymorph at  $P > 3.4$  GPa. The calculation of fluid isopleths ( $X_{\text{CO}_2} = \text{CO}_2/\text{H}_2\text{O}+\text{CO}_2$ ;  
972  $X_{\text{CH}_4} = \text{CH}_4/\text{H}_2\text{O}+\text{CH}_4$ ) has been performed using the Perple\_X and the EoS of Connolly and  
973 Cesare (1993). Reference buffers FMQ, hematite–magnetite (HM), wustite–magnetite (WM), iron-  
974 wustite (IW) and quartz–iron–fayalite (QIF) are shown for reference. Fluids in equilibrium with  
975 graphite buffered at FMQ conditions become increasingly enriched in  $\text{CO}_2$ , which reaches its  
976 maximum concentration at about 100 km depth, where FMQ and CCO almost converge. (B)  
977 Cartoon showing the fate of organic matter in subduction zones. Disordered organic matter  
978 contained in marine sediments undergoes partial to complete graphitization by increasing  
979 subduction temperature. Experimental results and thermodynamic models presented in this study

980 indicate that disordered carbon is more prone to oxidation with respect to crystalline carbon  
981 especially at low pressures, characterizing the forearc region. At these depths, an intense flush of  
982 water would be able to dissolve selectively disordered organic matter from the subducted  
983 sediments, while graphite behaves in a more refractory manner. This differential dissolution  
984 susceptibility is expected to progressively decrease as subduction proceeds, vanishing at about 100  
985 km depth where the difference in free energy between graphite and disordered carbon tends to zero.

986

#### 987 **Electronic Annex**

988 Supplementary Table 1: thermodynamic data for graphite (gph), glass-like carbon type I (GC;  
989 preferred model) and diamond (diam), formatted for Perple\_X package  
990 (<http://www.perplex.ethz.ch>) and to be copy-pasted in the used thermodynamic database file. Heat-  
991 capacity function and thermal expansion of glass-like carbon assumed identical to graphite.  
992 Diamond data after Day (2012). See also Table 4 and text for details.

993 Supplementary Figure 1: Thermodynamic model of FMQ and NNO buffers, calculated with  
994 Perple\_X and the hp04ver.dat database.

995 Supplementary Figure 2: Electron microscope images of the starting materials. (a) back-scattered  
996 electron image of graphite; (b) back-scattered electron image of glass-like carbon.

997 Supplementary Figure 3: Synchrotron X-ray powder diffraction of graphite, char and glass-like  
998 carbon.

999 Supplementary Figure 4: Raman spectra of polished and unpolished graphite used as starting  
1000 material, and of polished graphite quenched from experimental conditions.

1001 Supplementary Figure 5: Raman spectra of char obtained from high-pressure decomposition of  
1002 glucose at 1 GPa–800°C after 12h and 24 h.

1003 Supplementary Figure 6: Composition of the fluids from decomposed glucose, measured by using  
1004 the capsule-piercing technique and plotted on ternary C–O–H diagram.